Journal of Inorganic and Organometallic Polymers and Materials
https://doi.org/10.1007/s10904-025-03666-y

RESEARCH

Lead-Free Double Halide Perovskite Compounds: Unveiling the Structural, Optoelectronic, and Transport Properties of A_2TlRhF_6 (A = K, Rb) for Robust and Sustainable Green Energy Applications

Abrar Nazir[1] · Arti Saxena[2] · Ejaz Ahmad Khera[1] · Mumtaz Manzoor[3] · Ramesh Sharma[4] · Ahmed Ahmed Ibrahim[5] · Mohammed A. El-Meligy[6,7] · Barno Abdullaeva[8]

Received: 21 December 2024 / Accepted: 14 February 2025

Abstract

The structural, optoelectronic, and thermoelectric features of A_2TlRhF_6 (A=K, Rb) have been computed using the most versatile DFT-dependent FP-LAPW method. The calculated structural parameters, including formation energy, tolerance factor, and energy versus optimized volume plots, provide clear evidence of the structural and thermodynamic stability of the studied compounds. The results of band structure and density of states (DOS) reveal that studied compounds are semiconducting materials. The energy band gap of 2.98 eV and 2.97 eV has been found for K_2TlRhF_6 and Rb_2TlRhF_6 respectively. The optical properties of the compounds are studied with incident photon energy. The maximum absorption and minimum reflectivity and loss explore its effective application in optical devices. The compounds absorption in the UV-visible range makes them ideal candidates for solar cells. In addition, transport properties are examined in detail, demonstrating significant dependence on temperature and chemical potential as demonstrated by the assessed thermoelectric parameters. In order to evaluate the transport features versus the chemical potential and temperature, the power factor (PF), thermal conductivity, figure of merit, electrical conductivity, and Seebeck coefficient are computed. Our outcomes can be useful for future experimental studies to evaluate A_2TlRhF_6 (A=K, Rb) for applications involving energy from renewable sources.

Keywords DFT · Perovskite · mBJ · Optoelectronic · Thermoelectric properties

1 Introduction

Over recent years, the quest for sustainable energy solutions and advanced energy conversion technologies has led to a surge in research across various sectors [1]. Among these, thermoelectric compounds proficient of directly transforming heat into power and vice versa, have emerged as a focal point for innovation in power generation and cooling systems [2]. The escalating demand for electrical appliances, coupled with rising greenhouse gas emissions from air

---

✉ Ejaz Ahmad Khera
ejaz.khera@iub.edu.pk

✉ Ramesh Sharma
sharmadft@gmail.com

[1] Department of Physics Bahawalnagar Campus, The Islamia University of Bahawalpur, Bahawalpur 63100, Pakistan

[2] Department of Electronics & Communication, Pranveer Singh Institute of Technology, Kanpur, U.P, India

[3] Institute of Physics, Slovak Academy of Science, Dubravska Cesta 9, 84507 Bratislava, Slovakia

[4] Department of Applied Science, Feroze Gandhi Institute of Engineering and Technology, Raebareli, India

[5] Department of Physics and Astronomy, College of Science, King Saud University, P.O. Box 2455, 11451 Riyadh, Saudi Arabia

[6] Jadara University Research Center, Jadara University, PO Box 733, Irbid, Jordan

[7] Applied Science Research Center, Applied Science Private University, Amman, Jordan

[8] Department of Mathematics and Information Technologies, Vice-Rector for Scientific Affairs, Tashkent State Pedagogical University, Tashkent, Uzbekistan

conditioners and refrigerators, has exacerbated the global energy crisis. In response, efforts have been made to explore alternatives that can address this growing energy demand and alleviate environmental concerns [3]. Renewable energy technologies, including solar panels, wind energy, hydrogen fuel cells, and biomass, have been recognized for their potential to tackle the twin challenges of energy scarcity and environmental degradation [4]. Thermoelectric materials, in particular, are attracting attention for their unique ability to harness waste heat from industrial processes and convert it into valuable electrical energy. This approach to power generation, leveraging thermoelectric technology, holds the promise of significantly enhancing the efficiency of energy conversion systems by repurposing otherwise discarded heat energy into a useful electrical form [5].These devices are pivotal in the direct conversion of heat into electricity and have been the focal point of extensive research aimed at addressing thermal pollution and mitigating energy scarcity. They are seen as key contributors to fostering a sustainable and comfortable future environment [6]. The role of thermoelectric-based power generation (TEG) is pivotal in transforming excess heat energy into electrical power. This alternative, eco-friendly technology is key to converting waste-heat energy into electricity, thereby boosting the overall efficiency of energy conversion systems [7]. A functions by leveraging the Seebeck effect (S), which elucidates how a temperature differential (T) across a thermoelectric material creates a potential difference, propelling charge carriers within a circuit [8]. The efficiency of thermoelectric materials is encapsulated by the figure of merit. This formula represents the balance between thermal and electrical transport, where S denotes the Seebeck coefficient, σ is electrical conductivity, κ stands for thermal conductivity, and T represents temperature [9, 10]. The pursuit of high ZT values involves optimizing these variables to enhance material efficiency for thermoelectric applications. Thermoelectric generators allow heat to converted directly into they have been the subject of extensive research on electricity [11–14]. TEGs are consequently anticipated to lessen thermal pollution and energy shortages. They will contribute to creating a comfortable atmosphere going forward. A crucial phase in the production of clean, renewable energy is the conversion of heat into electrical energy using thermoelectric genera tors. The Seebeck coefficient has been used to demonstrate the potential gradient between various thermoelectric material interactions. [15–16].

Recent advancements in TEG technology have highlighted the potential of vacancy-ordered double perovskites, such as K_2PtCl_6, as promising thermoelectric materials. These compounds are gaining attention as viable alternatives to lead halide perovskites, offering non-toxicity, flexibility, reliability, wide carrier diffusion lengths, tunable band gaps, and robust air stability [17, 18]. Their appeal is further magnified by their flat valence bands, which are conducive to effective thermoelectric performance. Research into vacancy-ordered double perovskites has unveiled materials with outstanding thermoelectric properties. Investigations by Huma et al. [19] on Cs_2SnI_6 and Rb_2SnI_6, and by Mahmood et al. on Cs_2GeCl/Br_6 [20] have reported promising power factor (PF) and ZT values. Theoretical explorations by Ullah et al. have proposed K_2OsCl_6 and K_2OsBr_6 [21] as potential thermoelectric materials, alongside calculations that underscore the thermoelectric virtues of Cs_2NbI_6 [22]. Lot of double perovskites was employed such as Rb_2TlRhF_6 [23], A_2YAuI_6 (A = Rb, Cs) [24], A_2GeSnF_6 (A = K, Rb, Cs) [25] for thermoelectric applications. Qaid et al. explored the physical properties of Rb_2XRhF_6 (X = Li, Ag) employing DFT for renewable energy appliances [26]. A lot of perovskites, including Rb_2ASbX_6 (A = Tl, Cu & X = I, Cl) [27], $AcXO_3$ (X = Cr, Fe) [28], $Cs_2BB'F_6$ (B = Rb, In, Na and B' = Ir, As, Rh) [29], $K_2NaGaBr_6$ and $K_2RbTlBr_6$ [30], and K_2TlAsX_6 (X = Cl, Br) [31], for optoelectronic and renewable applications by using density functional theory. Different perovskites compounds such as, $RbMO_3$ (M = Np, Pu) [32], Cs_2MGaBr_6 [33], K_2GeNiX_6 (X = Br, I) [34], A_3XN (A = Co, Fe; X = Cu, Zn) [35], K_2GeMnX_6 (X = Cl, Br, I) [36], A_2CuMCl_6 (A = K, Rb; M = Sb, Bi) [37], Ba_2AlNbO_6 [38], K_2PtBr_6 [39] were utilized for energy harvesting applications. Mishra et al. explore the structural and optoelectronic features of Ca_3SbCl_3 halide perovskite by DFT for solar cell applications [40]. A number of composites are studied such as $Cs_2LiInBr_6$ [41], Ca_3SbBr_3 [42], Cs_2CuSbH_6 (H = Cl, Br, I) [43], Ca_3AsCl_3 [44], Mg_3AsCl_3 [45], Sr_3PnCl_3 (Pn = P, As, Sb) [46], Mg_3AsBr_3 [47] for energy applications using density functional theory.

This study explore A_2TlRhF_6 (A = K, Rb) double perovskite compounds, which have a comparable chemical composition and structure to previously reported double perovskites, to identify high-ZT materials. This indicates that our computed outcomes have comparable electrical and structural characteristics. These materials may have distinctive characteristics such as low effective masses and excellent carrier mobility, making them advantageous for electrical and thermoelectric uses. As per our understanding very limited work on these compounds. The goal of this effort is to enhance the thermoelectric capabilities of double perovskites by substituting the K and Rb atoms for the A atom. We have thoroughly explored the optoelectronic, structural and transport properties of A_2TlRhF_6 (A = K, Rb) by DFT. The studied compounds are categorized as Fluoro perovskites due to their fluoride-based anionic composition, specifically the presence of fluorine atoms in their crystal structure. Our results will inspire the researchers and scientists to experimental manufacture the devices based on A_2TlRhF_6 (A=K, Rb) perovskites.

2 Computational Methodology

This study determined the structural, thermoelectric, and optoelectronic features for A_2TlRhF_6 (A=K, Rb) using the most versatile DFT-dependent FP-LAPW [48] approach, which has been utilized on the basis of the WEIN2K code [49]. Moreover, we have applied the generalized gradient approximation (GGA) through the Perdew-Burke-Ernzerhof (PBE) procedure to figure out the exchange-correlation capability of the double perovskite (DP) bulk structure [50]. To investigate their electronic structures, such as the bulk modulus, ground state lattice constants, and space group, the cubic phase of the materials under investigation has been adjusted. Ground-state characteristics might be computed at the time optimization level by using energy discharges in the Murnaghan equation of state [51]. Energy optimization in the 10^4 Ry range lowered the strain tensions between atoms. The mBJ potential with and without SOC has also been employed for analyses of the electronic characteristics of the examined materials [52]. The waveform was generated using the basis of plane waves, an average number of the reciprocal mesh vector cut-off, and R_{MT}^{min}, which denotes the minimum radius of the muffin-tin sphere (RMT). The R_{MT} for atoms was set to the maximum value that could be achieved, i.e., $R_{MT}^{K/Rb} = 2.5$, $R_{MT}^{Tl} = 2.2$, $R_{MT}^{Rh} = 2$, and $R_{MT}^{F} = 1.8$ to avoid atomic sphere overlap. To achieve convergence, a strongly dense mesh with 100k points was applied to the specimen in the Brillouin Zone (BZ). Specifically, the convergence of charge and energy among successive cycles produced values like 0.0001e and 0.0001Ry, which improved the results. Optical properties have been evaluated using Kramers-Kronig relations which is given as,

$$\varepsilon_1(\omega) = 1 + \frac{2p}{\pi}\int_0^\infty \frac{\acute{\omega}\varepsilon_{2(\acute{\omega})}}{\left(\omega^{'2} - \omega^2\right)} d\acute{\omega} \tag{1}$$

The optimized electrical configurations using mBJ and the convergent energy have been utilized to compute the charge transport features by means of the Boltztrap algorithm [53], which is based on Boltzmann-transport theory. A fine grid mesh (42 × 42 × 42) has been used for the thermoelectric characteristics computation. The thermoelectric figure of merit was computed by the given formula,

$$\mathrm{ZT} = S^2\frac{\sigma T}{K} \tag{2}$$

3 Results and Discussion

3.1 Structural Properties

The crystal structures of the compounds A_2TlRhF_6 (A=K, Rb) with space group Fm-3 m #225 were employed for all calculations. The atomic positions for A_2TlRhF_6 (A=K, Rb) are Rb/K (0.25, 0.25, 0.25), F (0, 0, 0.21850), Tl (0, 0, 0.5) and Rh (0, 0, 0). Figure 1 presents the crystal structure of A_2TlRhF_6 (A=K, Rb). It is made up of 12 stacked F atoms separating the two octahedra, TlF_6 and RhF_6. These octahedra create spaces in which K/Rb atoms position themselves. Inside the structure, this octahedral spinning pattern remains constant. The parabolic energy versus volume plots, shown in Fig. 2, is the result of fitting data on energy into the Murnaghan equation [51] of state for determining the ground state energy. For structural stability, we have computed the tolerance factor of the examined compounds. The ground state energy and tolerance factor are represented as follows:

$$E_{tot}(V) = E_o(V) + \frac{B_o V}{\acute{B}\left(B^{'} - 1\right)}\left[B\left(1 - \frac{V_o}{V}\right) + \left(\frac{V_o}{V}\right)^{\acute{B}} - 1\right] \tag{3}$$

To assess the ingredient's stability while preserving overall stability, the tolerance factor (τ) is computed [54, 55].

$$\tau = \frac{\mathrm{r_A} + \mathrm{r_x}}{\sqrt{2}\left(\frac{\mathrm{r_{Rh}} + \mathrm{r_{Tl}}}{2} + \mathrm{r_x}\right)} \tag{4}$$

Here r_A, r_{Rh}, r_{Tl}, and r_X represent the radius of K/Rb, Rh, Tl and F atoms respectively. For stable cubic perovskites, Goldsmith's criteria usually approach unity under ideal conditions. Specifically, the calculated tolerance factors for A_2TlRhF_6 (A=K, Rb) are 1.003 and 1.06, respectively, which confirm the structural stability of these compounds within the ideal range [56]. Our calculated values are displayed as lines in the aforementioned range in Table 1. The materials under consideration are therefore stable in their cubic configuration. The following equation was used to determine the formation energy in order to verify the thermodynamic stability:

$$\mathrm{E_F} = \frac{\mathrm{E_{K/Rb}TlRhF_6} - \left(2\mathrm{E_{K/Rb}} + \mathrm{E_{Tl}} + \mathrm{E_{Rh}} + 6\mathrm{E_F}\right)}{10} \tag{5}$$

It is evident from Table 1's negative formation energy estimates that the materials on the mentioned list are thermally stable and acceptable for synthesis [57, 58].

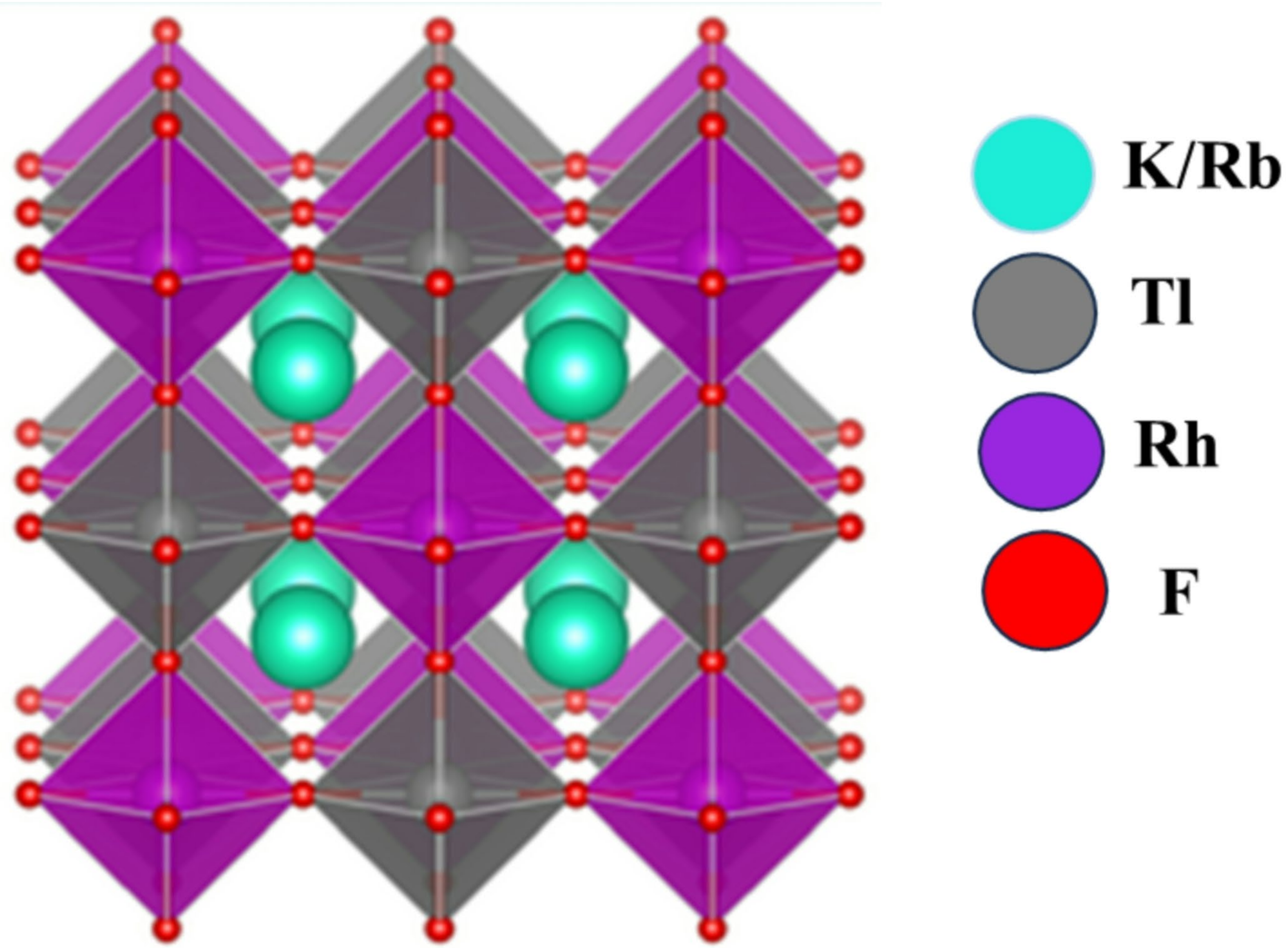

Fig. 1 Crystal structure of double perovskites A_2TlRhF_6 (A=K, Rb)

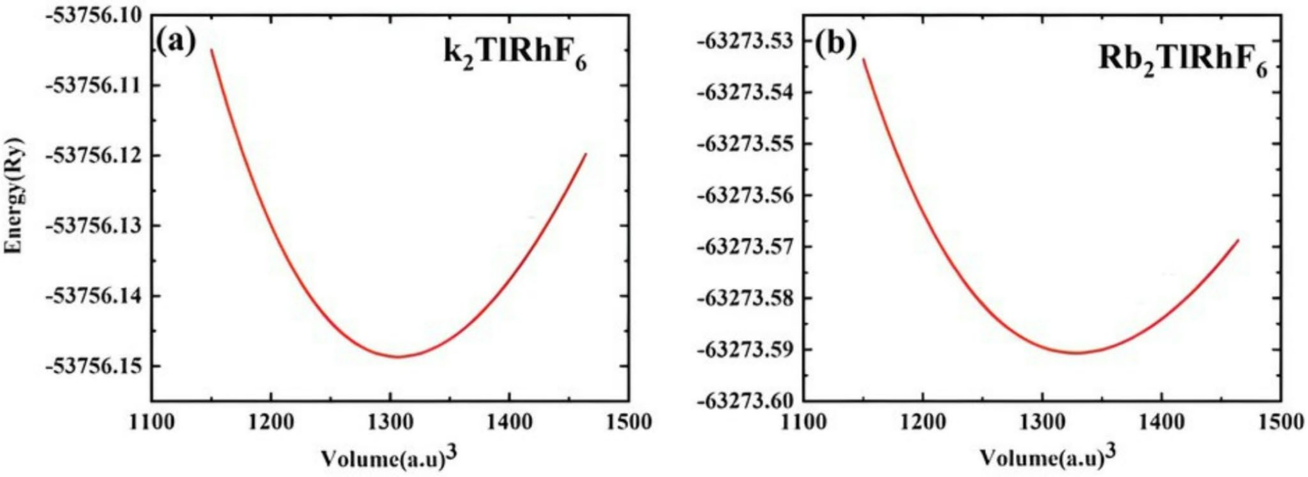

Fig. 2 Energy versus volume optimization curves of **a** K_2TlRhF_6**b** Rb_2TlRhF_6

Table 1 Calculated lattice parameter *a* (A°), bulk modulus *B*, its derivative B_P, the minimum total energy E_{tot}, formation energy E_f and tolerance factor

XC	a (Å)	V (a.u^3)	B (GPa)	B.P	E_{tot}(Ry)	E_f(eV/atom)	Tolerance factor
K_2TlRhF_6	9.18	1306.86	54.71	4.21	– 53756.148	– 2.35	1.003
Rb_2TlRhF_6	9.23	1328.03	54.68	4.24	– 63273.590	– 2.343	1.06
Others work [23]	9.26	1339.6	46.9	5	– 63273.500		

3.2 Electronic Properties

Electronic properties refer to the characteristics and behaviors of majority charge carriers in materials, including their energy levels, mobility, conductivity, and interactions. Electronic properties include the study of the band structures along with their density of states (DOS) [59]. The band structure describes the distribution of electronic bands in a material. It determines whether a material is an insulator, conductor and semiconductor. The distribution of available states of charged particles in a material at diverse energy levels can be described by its DOS. It provides details on how many states are present at a specific energy.

We have computed the band structure of A_2TlRhF_6 (A = K, Rb) double perovskites by using the TB-mBJ and mBJ + SOC potentials to examine the electronic structure characteristics as shown in Fig. 3a–d. The band gaps of 3.02 eV and 2.99 eV has been detected for K_2TlRhF_6 and Rb_2TlRhF_6, respectively, by Tb-mBJ potential. The purpose of employing SOC is to get precise band gap measurements in relation to experiment-derived values [60]. For this reason, we examined the band gaps corresponding to K_2TlRhF_6 (E_g = 2.98 eV) and Rb_2TlRhF_6 (E_g = 2.97 eV) by using mBJ + SOC. It is significant to note that both tested compounds have a direct band gap because conduction band minima CBM and valance band maxima VBM take place at the "L-L" symmetry points. Interestingly, direct band gap compounds are more favorable for solar cell applications. In another study the band gap of $Rb_2TlRhF_6$was found 3.2 eV which is tabulated in Table 2. Therefore, the compounds under consideration could be utilized to produce solar energy cells. As the atomic numbers of A (K, Rb) have grown, the band gap has been mitigated. This can be related to the familiar inter-site exchange interactions. The number of orbital overlaps that coincide has a direct correlation with this and scales inversely with the lattice constants [24]. While in another study, band gap of Rb_2TiCl_6 was found to be 2.99 eV by mBJ and 2.94 eV by mBJ + SOC potential [61]. Murtaza et al. found the indirect band gap of 0.9 and 1.95 eV for $RbInBr_3$ and $RbInCl_3$ respectively [62].

The computed outcomes of the total density of states are portrayed in Fig. 4a, b. In order to confirm the results of the band structure, the total density of states (TDOS) has been calculated. For both the PDOS and TDOS diagrams, the Fermi level is represented by a vertical dashed line. The energy charts show values between − 10 and 10 eV. States in the valence band (VB) are found at negative energy, whereas states in the conduction band (CB) are visible at positive energy. TDOS displays the total number of distinct states in both the conduction and valence bands. The valence band is enriched with the F states, as depicted in Fig. 4. From TDOS plots, most of the energy states are found in valance band VB. It is worth mentioning that the results of TDOS are in route with the band structure outcomes.

The computed outcomes of the partial density of states are illustrated in Fig. 5a, b. For K_2TlRhF_6, the valance band is formed due to the hybridization of Rh-*4d* and F-*2p* and the minimal contribution of Tl-*6s* states. The conduction band is formed with Rh-*4d* states and electrons from Tl-*6p* orbitals, and the energy states of K are found away from the Fermi level, as portrayed in Fig. 5a. Figure 5b demonstrates that Rh-*4d* orbitals, Rb-*d*, and Tl-*6s* states make up the conduction band of Rb_2TlRhF_6. Moreover, the V.B is formed owing to the hybridization of Tl-*6s*, Rh-*4d*, and F-*2p* states, as indicated in Fig. 5b.

3.3 Optical Properties

In order to comprehend the critical significance of the proposed material for optoelectronics and its uses in solar cells, its optical characteristics were thoroughly investigated. We analyzed the optical enactment of the evolution between the valence and conduction bands. The optical characteristics that materials possess are revealed by their interaction with light.

One important variable that helps explain how a material reacts to electromagnetic radiation is the complex dielectric function ε (ω) [63]. It combines contributions from lattices and electronic systems. Dielectric function is given as,

$$\varepsilon\left(\omega\right)=\varepsilon_1\left(\omega\right)+i\varepsilon_2\left(\omega\right) \tag{6}$$

The real portion accountable for enlightening the electronic polarizability is symbolized by $_1$ (), although the imaginary part associated to the materials electronic absorption of incident radiations is designated by ε_2 (ω). The most well-known Kramers-Kronig equations [64] link the dielectric function's real and imaginary aspects.

The imaginary part is given as,

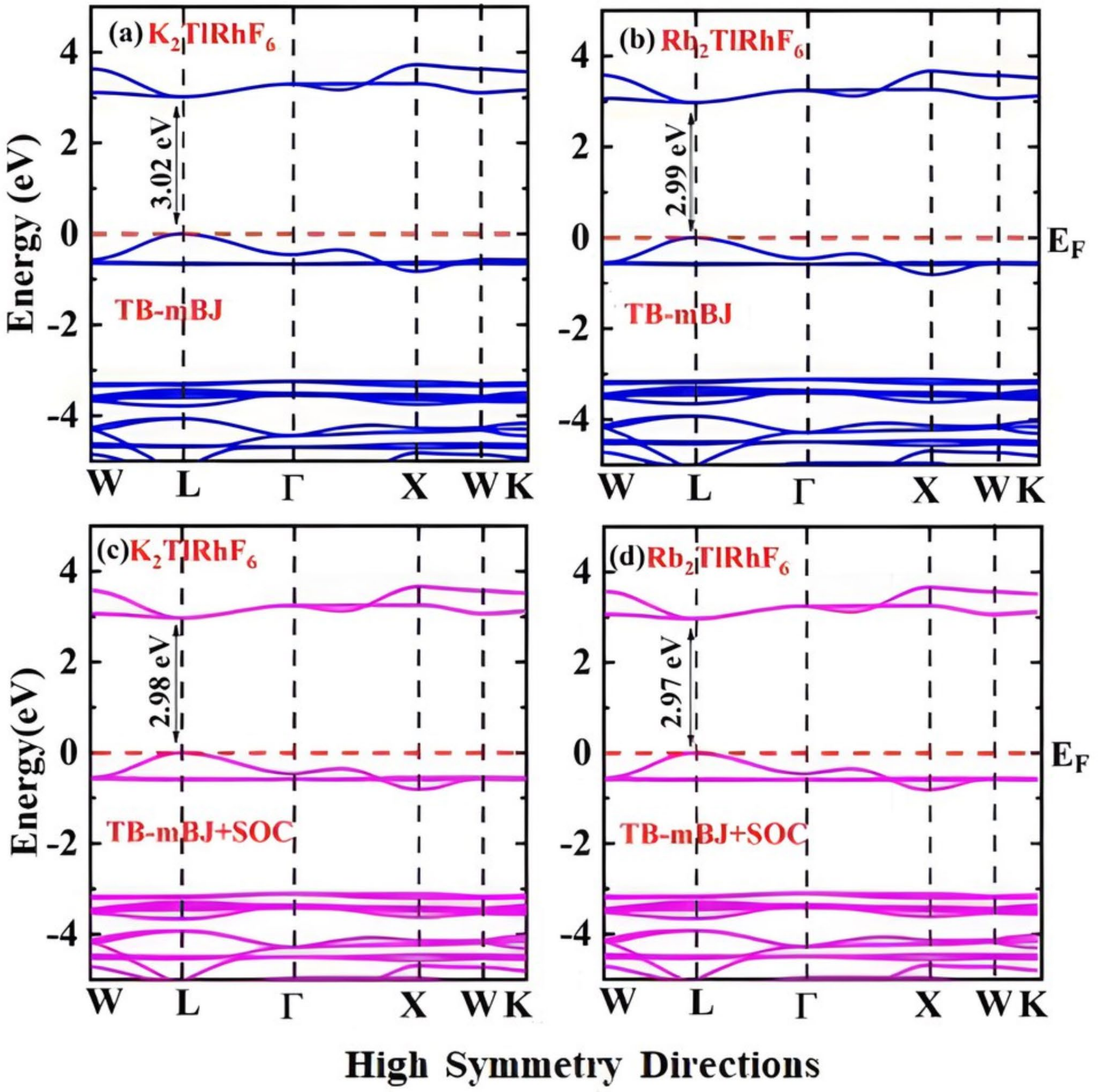

Fig. 3 Representations of the band structures of **a** K_2TlRhF_6 **b** Rb_2TlRhF_6 using the TB-mBJ and TB-mBJ + SOC approximation

Table 2 Calculated energy bandgap (in eV) by different potentials mBJ and mBJ + SOC

Properties	Tb-mBJ	mBJ + SOC	Others work [23]
K_2TlRhF_6	3.02	2.98	
Rb_2TlRhF_6	2.99	2.97	3.2

$$\varepsilon_2\left(\hbar\omega\right) = \frac{2\pi e^2}{\Omega\varepsilon_o}\sum\left|\psi_k^c\right| u.r \left|\psi_k^v\right|^2 \delta\left(E_k^c - E_k^v - E\right) \tag{7}$$

The calculated results of the complex dielectric CD constant ε (ω) are represented in Fig. 6a, b. The peak values of real dielectric function are 4.89 at 3.11 eV for K_2TlRhF_6 and 4.97 at 3.07 eV for Rb_2TlRhF_6. The static values ε_1 (0) are found to be 2.17 and 2.21 for K_2TlRhF_6 and Rb_2TlRhF_6, respectively. Remarkably, static function value ε_1 (0) and highest value of ε_1 (ω) of Rb_2TlRhF_6 is superior owing to slighter energy band-gap as compared to K_2TlRhF_6 compound. Several double perovskites exhibit comparable behaviour as reported [24, 25]. The energy band gaps and dielectric constant are correlated by Pens model [65] as given as;

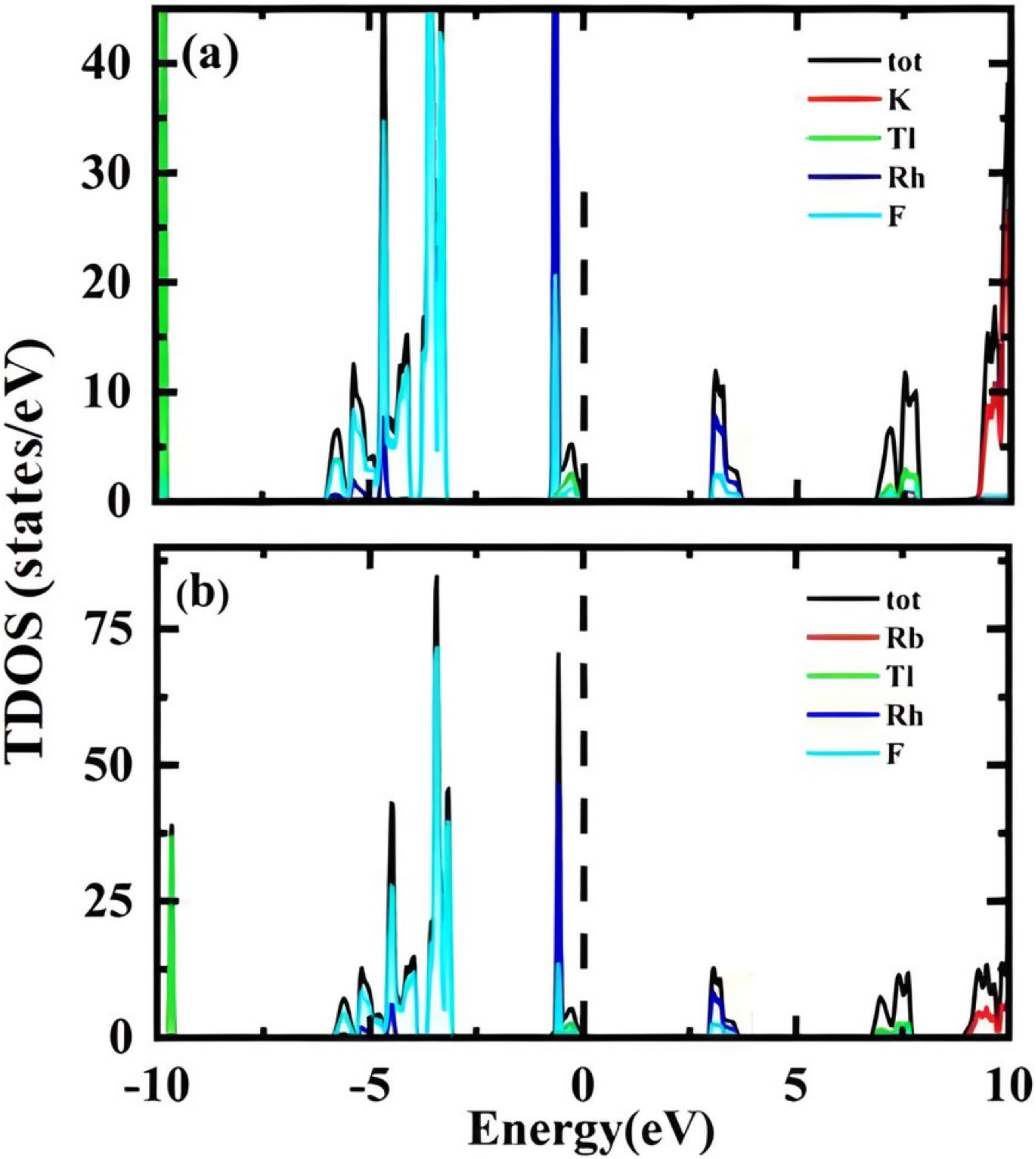

Fig. 4 Representations of the TDOS of **a** K_2TlRhF_6 **b** Rb_2TlRhF_6 using the Tb-mBJ approximation

$$\varepsilon_1\left(0\right)\approx 1+\left(\hbar\omega_p/E_g\right)^2 \tag{8}$$

Figure 6b shows the plot of the imaginary dielectric constant for the examined A_2TlRhF_6 (A=K, Rb) double perovskites. The extreme values of ε_2 (ω) are 4.71 at 3.36 eV (K_2TlRhF_6) and 4.74 at 3.33 eV (Rb_2TlRhF_6).

The amount of light which can travel through a substance depends on its refractive index. A substance's refractive index measures how light react with it [66]. Extraordinary refractive indices allow light to enter materials more gradually, which origins a correspondingly larger alteration in the route of the light inside the substance. Figure 5c displays

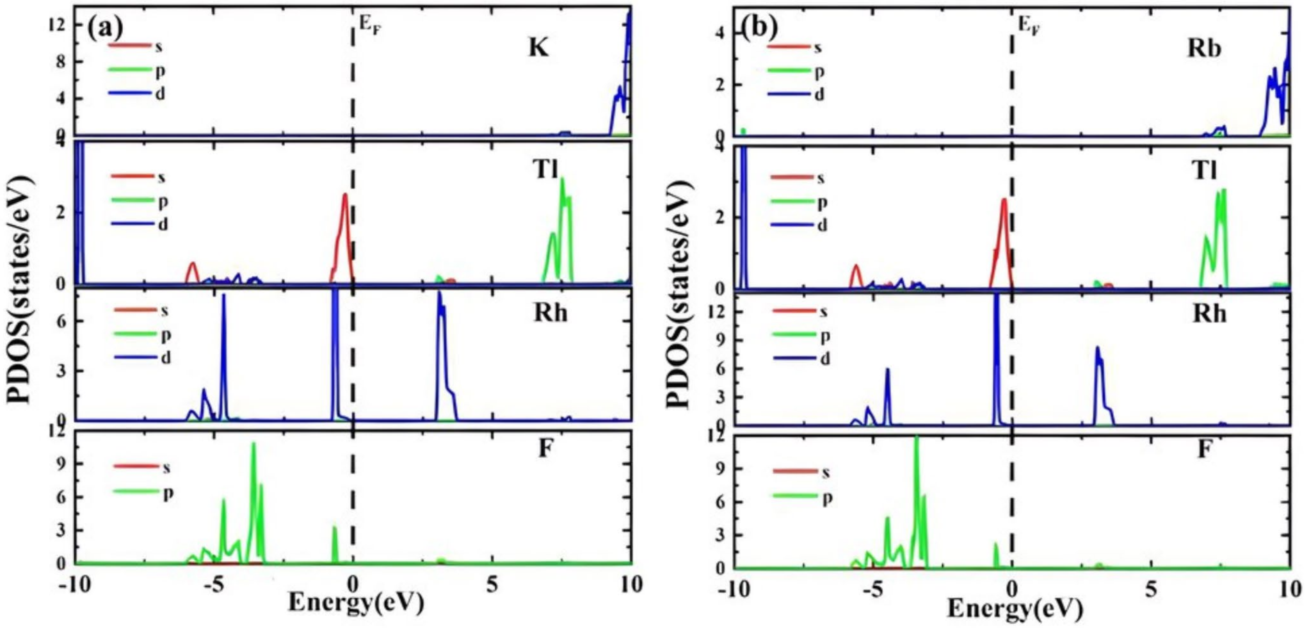

Fig. 5 Representations of the PDOS of **a** K_2TlRhF_6**b** Rb_2TlRhF_6 using the Tb-mBJ approximation

the calculated refractive indices for the examined double perovskites. The static $n(0)$ values are tabulated in Table 3. The maximum value of n (ω) is perceived to be 2.27 at 3.15 eV (K_2TlRhF_6) and 2.29 at 3.13 eV (Rb_2TlRhF_6).

The computed results of the extinction coefficient K (ω) are displayed in Fig. 6d. We analyze the extinction coefficient K (ω) of the A_2TlRhF_6 (A=K, Rb), with a focus on incoming photon energies in the range of 0 to 10 eV. The K () is a measurement that shows how well a substance reflects or absorbs light or radiation at a particular wavelength of light. The peak values of K () are witnessed at 3.55 eV and 3.54 eV for $K_2TlRhF_6$and Rb_2TlRhF_6 respectively.

The simulated outcomes of conductivity σ (ω) are portrayed in Fig. 7a. The electronic conduction is due to optical conductivity σ (ω). The optical conductivity is given as,

$$\sigma\left(\omega\right)=\ \frac{\omega}{4\pi}\mathrm{Im}\varepsilon\left(\omega\right) \tag{9}$$

For K_2TlRhF_6, the supreme computed σ (ω) is 3554 $(\Omega.m)^{-1}$ at 7.85 eV, for Rb_2TlRhF_6 3806 $(\Omega.m)^{-1}$ at 7.63 eV. Figure 7a indicates that σ (ω) values are zero underneath the optical band gap, indicating that charge carriers require greater anticipation to engage in electrical transport. The charge carriers become excited by the photon, whose energy equals the optical band-gap from which σ (ω) acquires its values. When photons of a suitable frequency happen on a material surface, σ (ω) likewise unveils the same pattern as ε_2 (ω).

The absorption coefficient α () of a substance indicates how much light it absorbs. The estimated results of absorption coefficient of A_2TlRhF_6 (A=K, Rb), are presented in Fig. 7b. To find the absorption coefficient, use the following relation:

$$I\left(\omega\right)=\frac{4\pi k\omega}{\lambda} \tag{10}$$

Figure 7b reveals that the maximum value of absorption for K_2TlRhF_6 is 109×10^4 cm^{-1} at 7.76 eV and Rb_2TlRhF_6 116×10^4 cm^{-1} at 7.98 eV, as observed. The first absorption peak has been observed for both compounds near the visible region. As demonstrated in Fig. 7b, it has been revealed that the examined compounds are capable of absorbing electromagnetic energy from the (UV-visible) with wavelengths of 160–522 nm for K_2TlRhF_6 and 155–523 nm for Rb_2TlRhF_6. This provides even more credibility to the applicability of these materials in the field of solar energy. According to optical absorption data, these compounds have the ability to absorb a broad spectrum of electromagnetic radiation, including UV-visible light, while maintaining their electrical properties. These results suggest that these compounds are useful in solar cells and optoelectronic applications.

Reflectivity is a crucial optical characteristic that quantifies the precise amount of incident light bounced off a material's surface in relation to the incident power [67]. Reflectivity can be calculated as,

$$R\ \left(\omega\right)\ =\frac{(n-1)^2+k^2}{(n+1)^2+k^2} \tag{11}$$

The anticipated reflectivity is presented in Fig. 7c. The reflectivity static values are tabulated in Table 3. Using this figure, the (R (0)) for A_2TlRhF_6 (A=K, Rb) have been

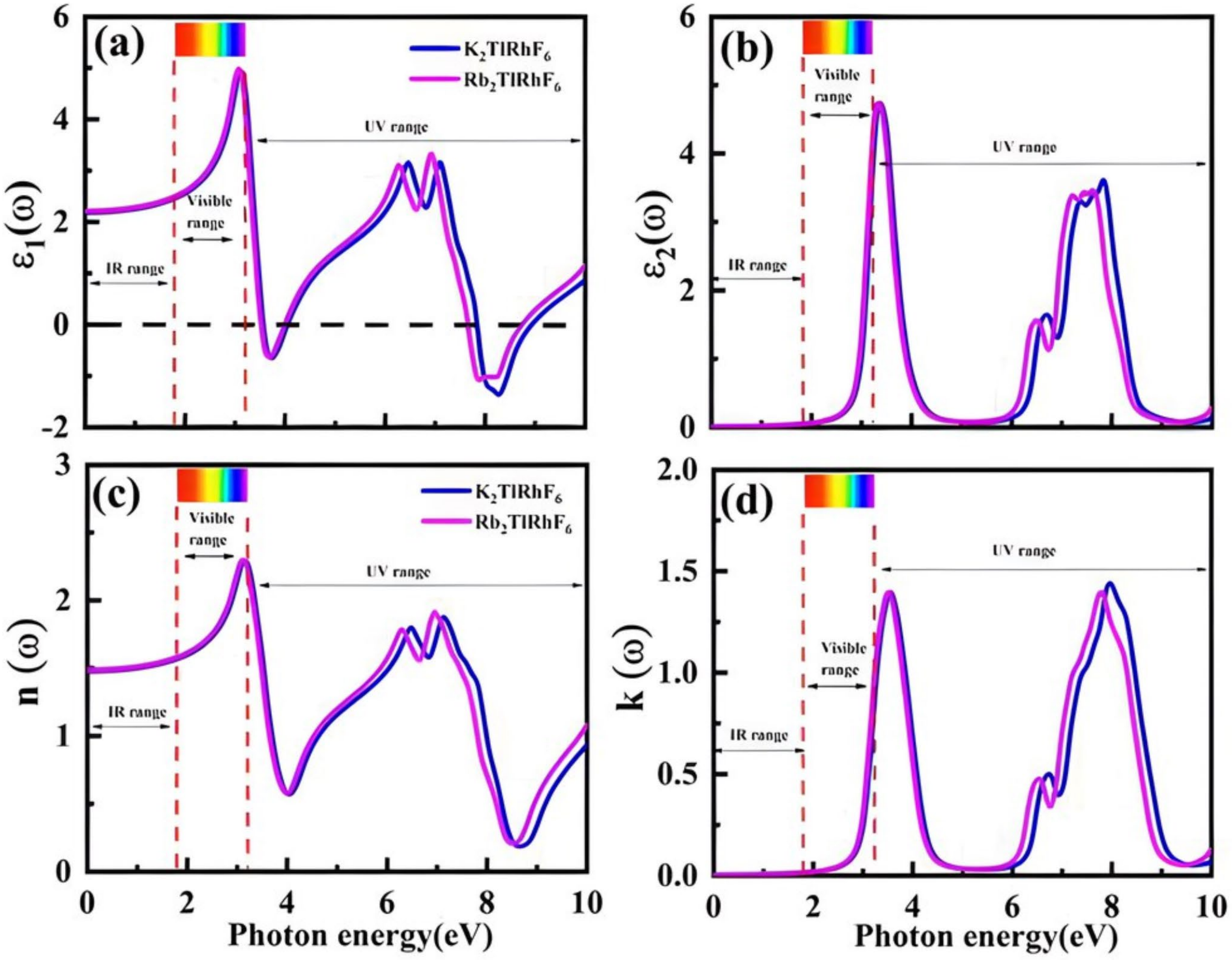

Fig. 6 The calculated energy dependent optical parameters **a** real part of the dielectric function **b** imaginary part of the dielectric function **c** refractive index coefficient and **d** extinction coefficient forA_2TlRhF_6 (A=K, Rb)

Table 3 Calculated optical and transport properties by Tb-mBJ potential

	Material property	K_2TlRhF_6	Rb_2TlRhF_6	Others work [23]
Optical properties	$\varepsilon_1(0)$	2.18	2.21	2.12
	n(0)	1.47	1.48	1.45
	R(0)	0.037	0.038	
Transport properties (300 K)	$\sigma/\tau(\Omega ms)^{-1}(10^{18})$	1.80	1.86	
	S(μVK)	247	244	
	k***l***(W/mK)	0.99	1.02	
	K_e (W/mKs)(10^{15})	0.043	0.043	
	k_{tot} (W/mKs)(10^{15})	1.03	1.06	
	PF$(10^{11}W/K^2ms)$	1.10	1.11	
	ZT	0.031	0.03	

estimated to be 5%. Values below 35% are found in the R (ω) observable range. This shows that the highest amount of visible photons may be absorbed by the investigated double perovskites A_2TlRhF_6 (A=K, Rb). Therefore, these compounds are suitable for the usage in solar cell tenders. The energy that a fast moving electron loses when passing through an ingredient is calculated using the loss function. The computed fluoro A_2TlRhF_6 (A=K, Rb) perovskites loss function is demonstrated in Fig. 7d. The region where absorption is most significant has very little energy loss. Two peaks have been identified in the specified energy range of 0–10 eV. In the visible zone, there is no energy loss. The greatest maximum levels of K_2TlRhF_6 and Rb_2TlRhF_6 are regarded as 8.93 eV and 8.73 eV, respectively.

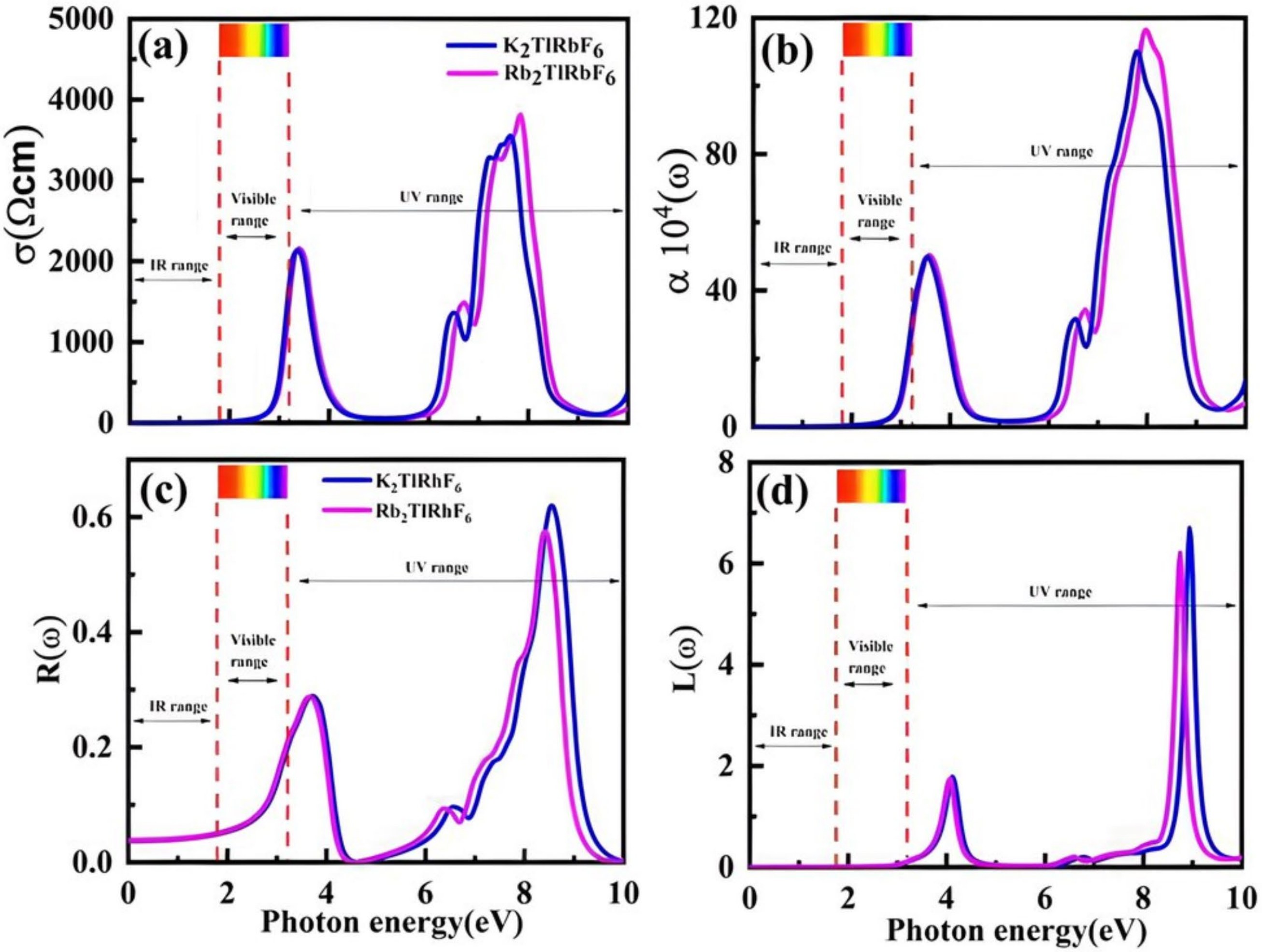

Fig. 7 The calculated energy dependent optical parameters **a** optical conductivity **b** absorption coefficient **c** optical reflectivity and **d** energy loss function forA_2TlRhF_6 (A=K, Rb)

3.4 Thermoelectric Properties

It is possible to convert excess heat into useful electrical energy by using thermoelectric materials. Perovskites are more appealing because of their affordability, low cost, excellent electrical conductivity, and environmental friendliness [68–70]. Therefore, in order to calculate the thermoelectric variables for A_2TlRhF_6 (A=K, Rb) double perovskites, which include power factor, lattice and thermal conductivities, figure of merit ZT, electrical conductivity and Seebeck coefficient. The BoltzTraP code coupled with Wien2k software has been employed to simulate the transport properties of the examined perovskites. The A_2TlRhF_6 (A=K, Rb) double perovskites thermoelectric TE characteristics are investigated in order to evaluate how well thermal energy can be transformed into electrical power. Employing TE materials, wasted heat energy can be changed into electricity to help solve the energy crisis and minimize pollution. The computed thermoelectric parameters at room temperature are tabulated in Table 3.

The Seebeck effect, which was discovered in 1821 by German scientist Tomas Joan Seebeck, is used to power thermoelectric generators. When a gradient of temperature is established between the two intersections, the Seebeck coefficient is used to measure the potential difference between both of the distinguishing conductors or semi-conductors. The Seebeck effect occurs when an object experiences a temperature gradient because charge carriers from the warmer, more heated region go to the colder, more concentrated area, increasing electron concentrations. The thermoelectric efficiency of the material is influenced by the potential gradient, which is determined by using the Seebeck coefficient (S) as a result of the two distinct contacts of metal temperatures. The simulated results of Seebeck coefficient against temperature are displaced in Fig. 8a. At room temperature, the values of Seebeck coefficients are 247μVK^{-1} and 244μVK^{-1} for

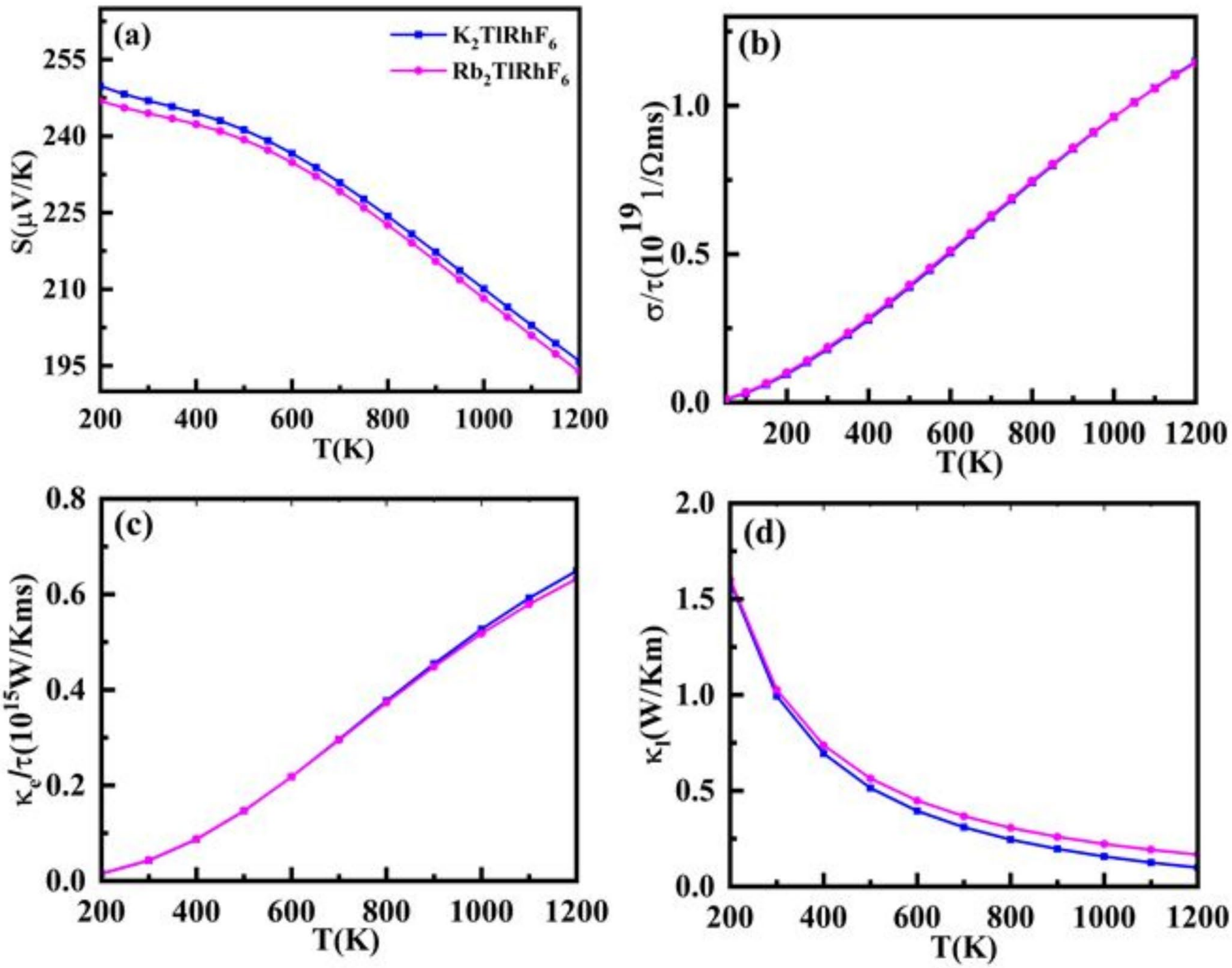

Fig. 8 Computed results of ofA_2TlRhF_6 (A=K, Rb) with temperature using the TB-mBJ approximation **a** seebeck coefficients **b** electrical conductivity **c** electronic thermal conductivity **d** lattice thermal conductivity

K_2TlRhF_6 and Rb_2TlRhF_6 respectively. Seebeck coefficient values below zero indicate n-type electrical transportation, while Seebeck coefficient values above zero indicate p-type behavior [63]. Because both examined compounds have a positive Seebeck coefficient ($S>0$), the results indicate that they are p-type materials [71].

The elevated electrical conductivity of both examined perovskite materials against temperature can be observed in Fig. 8b, which further indicates that the compound σ/ rises with temperature. Thermionic emission induces thermal energy to surpass the work function of substances in semiconductors, which explains why their electrical conductivity usually rises with temperature. The value of electrical conductivity rises with temperature, and both compounds show similar values of electrical conductivity up to 1200 K.

Figure 8c,d shows the simulated results of the electronic and lattice thermal conductivity of the analyzed A_2TlRhF_6 (A=K, Rb) perovskite compounds. According to Fig. 8c, the electronic thermal conductivity of K_2TlRhF_6 and Rb_2TlRhF_6 increases as the temperature goes up, reaching its highest value of 0.65×10^{15} W/mKs and 0.63×10^{15} W/mKs, respectively, at 1200 K. Interestingly, both double perovskites reveal similar values of κ_e at room temperature, as presented in Table 3. These estimated high values of electronic thermal conductivity are in line with the literature [72].

The Slacks model has been used to determine κ_l because the BoltzTraP algorithm considers that the phonon influence on thermal conductivity (κ_l) is negligible [73]. According to this model, one can determine κ_l in the following way:

$$\kappa l \ = B\frac{M\delta n^{1/3}\Theta_D^3}{T\gamma^2} \tag{12}$$

Where, γ represents Grüneisen parameter, M is molar mass, A is constant having value 3×10^{-8}, V is volume, Θ

$_D$ is Debye temperature and N is number of atoms in the unit cell. Figure 8d depicts that both compounds have a declining trend in lattice thermal conductivity with the rise in temperature. The value of κ_l is decreasing with temperature owing to the inversely relationship between temperature and lattice conductivity, which can be seen in Fig. 8d. At room temperature, the values of κ_l are 0.99 W/Km and 1.02 W/Km for K_2TlRhF_6 and Rb_2TlRhF_6, respectively.

One important thermoelectric property for figuring out the thermal performance of an ingredient is its power factor. Compounds that have a greater power factor (PF) often release less heat. The computed values of PF at room temperature are tabulated in Table 3. Moreover, with the rising temperature, the value of PF increases for both examined compounds, as depicted in Fig. 9a.The figure of merit (ZT) is a basic property of materials that is used to assess their thermoelectric performance [70, 74–81]. Greater ZT values imply thermoelectric properties that are more effective. The computed values of power factor at room temperature are presented in Table 3.

Figure 9b makes it evident that ZT values increase with temperature, and it is reasonable to assume that compounds with greater temperatures should have better thermoelectric properties. Interestingly, both examined compounds exhibit a similar value of ZT at room temperature.

Chemical potential is the amount of energy required for electrons in a circuit to overcome coulomb potential. The chemical potential is negative as well as positive. At Fermi level, this value is 0. The negative portion shows p-type behavior, and the positive portion shows the n-type response [78–79]. The computed Seebeck results against chemical potential are displaced in Fig. 10a, b. Figure 10a shows that the maximum value of S at 300 K for n-type K_2TlRhF_6 is 2849 µV/K at 0.77 eV. Moreover, when temperature rises from 300 to 1200 K, this value of S reduces. The value of S at 700 K is 2053 µV/K at 1.31 eV, and 1165 µV/K at 1.21 eV has been found for K2TlRhF6. The values of S for n-type Rb_2TlRhF_6 are 2846 µV/K (0.76 eV) at 300 K, 2024 µV/K (1.27 eV) at 700 K, and 1148 µV/K (1.20 eV) at 1200 K. The optimum Seebeck coefficient value has been observed by both of these materials around 300 K, and as temperature rises, this value starts to drop because of a surge in holes and electron conductivity caused by growing thermal energy [69]. The power factor plots for A_2TlRhF_6 (A=K, Rb) perovskite with respect to chemical potential can be seen in Fig. 10c, d. The graphs demonstrate that the smallest power factor for the compounds under consideration occurs at 300 K. The values of PF at 300 K are 4.29×10^{11} W/mK^2s and 4.26×10^{11} W/mK^2s for n-type K_2TlRhF_6 and Rb_2TlRhF_6, respectively. For the p-type region, the value of PF increases from 300 K to 1200 K. Interestingly, the n-type region shows a greater value of PF as compared to the p-type region, as depicted in Fig. 10c, d.

Moving electrons from hot to cold places results in the creation of electric current. Good-quality TE substances should have high electrical conductivity [80]. Figure 11a, b exhibits the electrical conductivity for K_2TlRhF_6 and Rb_2TlRhF_6 at 300 K, 700 K, and 1200 K in order to draw attention to their thermoelectric capabilities. For n-type K_2TlRhF_6, the values of electrical conductivity are $6.64\times10^{19}(\Omega ms)^{-1}$ (3.19 eV) at 300 K, $5.84\times10^{19}(\Omega ms)^{-1}$ (3.25 eV) at 700 K, and $4.97\times10^{19}(\Omega ms)^{-1}$ (3.30 eV) chemical potential at 1200 K. While Rb_2TlRhF_6 has electrical conductivity values of 6.42×10^{19} $(\Omega ms)^{-1}$ (3.12 eV), $5.64\times10^{19}(\Omega ms)^{-1}$ (3.17 eV), and $4.74\times10^{19}(\Omega ms)^{-1}$(3.22 eV) at 300 K, 700 K, and 1200 K, respectively. Moreover, our computed results show the values of electrical conductivity are higher for the n-type zone as compared to the p-type region, as depicted in

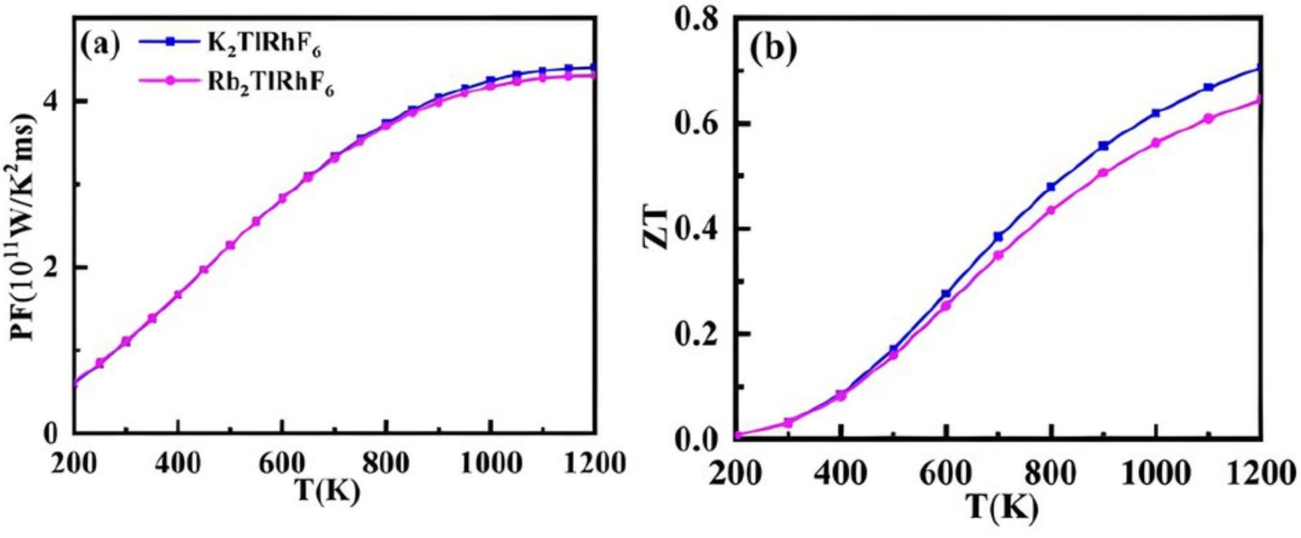

Fig. 9 Computed results ofofA_2TlRhF_6 (A=K, Rb) with temperature using the TB-mBJ approximation **a** power factor **b** figure of merit ZT

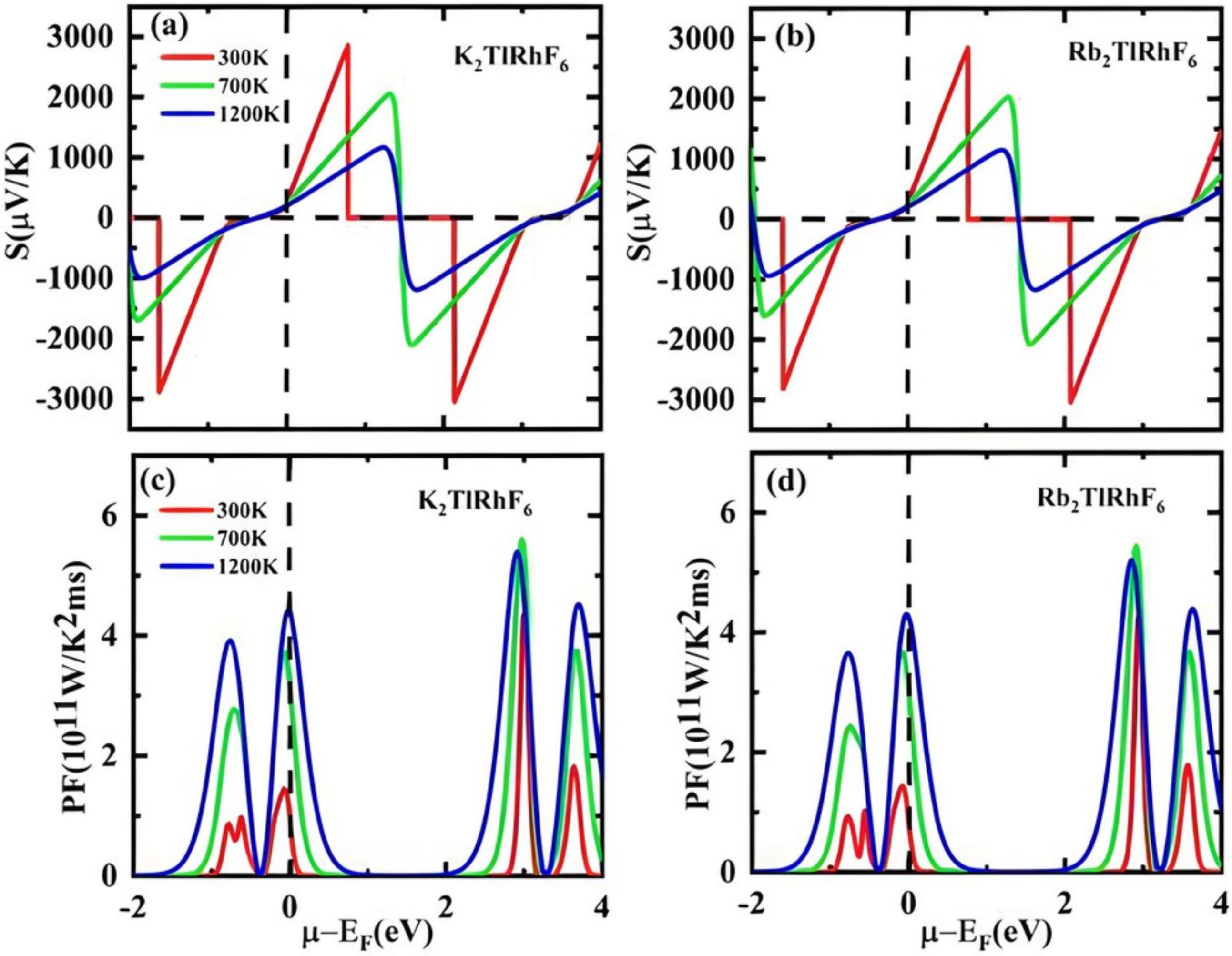

Fig. 10 Computed results ofA$_2$TlRhF$_6$ (A=K, Rb) with chemical potential using the TB-mBJ approximation **a** seebeck coefficients of K$_2$TlRhF$_6$**b** seebeck coefficients of Rb$_2$TlRhF$_6$**c** power factor of K$_2$TlRhF$_6$**d** power factor of Rb$_2$TlRhF$_6$

Fig. 11a, b. Furthermore, the findings conclusively demonstrate that electrical conductivity rises with chemical potential, verifying the previously published literature [81].

The ability of a material to transport heat via the transport of electrons and lattice vibrations is known as thermal conductivity. Low thermal conductivity with respect to the large temperature differences is a requirement for resources used in high-performance TE gadgets. Figure 11c, d presents the thermal conductivity for K$_2$TlRhF$_6$ and Rb$_2$TlRhF$_6$ as a function of chemical potential. The value of thermal conductivity rises with an increase in temperature. For K$_2$TlRhF$_6$, its values are 0.44×10^{15} W/mKs with a chemical potential of 3.27 eV, 0.76×10^{15} W/mKs (3.32 eV), and 0.78×10^{15} W/mKs (2.97 eV) at 300 K, 700 K, and 1200 K, respectively. For Rb$_2$TlRhF$_6$, thermal conductivity values of 0.43×10^{15} W/mKs (3.21 eV) for 300 K, 0.72×10^{15} W/mKs (3.24 eV) for 700 K, and 0.75×10^{15} W/mKs (2.90 eV) for 1200 K have been observed. Remarkably, the thermal conductivity values are higher in n-type zone as compared to p-type region as portrayed in Fig. 11c, d. The predicted outcomes show that these compounds have relatively small thermal conductivity amounts at 300 K, which progress with temperature, and look at their optimum level at 1200 K. This implies that these compounds are appropriate for room-temperature use in thermoelectric devices. It also indicates that electron energy improves with temperature.

The predicted results of figure of merit ZT are displaced in Fig. 12a, b for A$_2$TlRhF$_6$ (A=K and Rb) perovskites. Figure 12 reveals that the value of ZT increases with the rise in temperature from 300 K to 1200 K. The value of the figure of merit of 0.99 at a chemical potential of 0.66 eV and 0.99 (2.35 eV) for K$_2$TlRhF$_6$ and Rb$_2$TlRhF$_6$, respectively, at 300 K has been found. It is worth mentioning that for both compounds, the value of ZT reaches (~1) at 300 K, 700 K, and 1200 K.

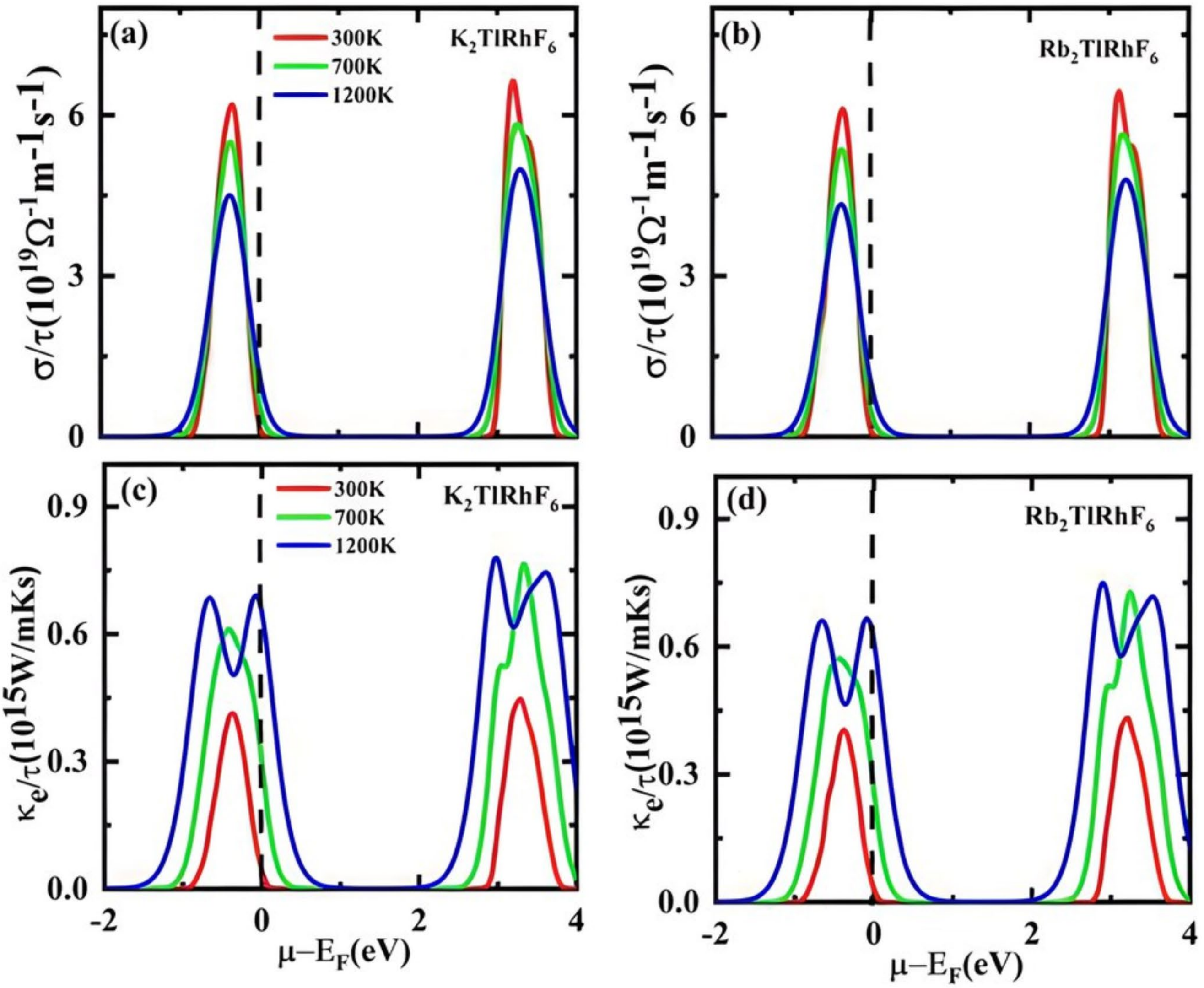

Fig. 11 Computed results of A_2TlRhF_6 (A=K, Rb) with chemical potential using the TB-mBJ approximation **a** electrical conductivity of K_2Tl-RhF_6**b** electrical conductivity of Rb_2TlRhF_6**c** electronic thermal conductivity of K_2TlRhF_6**d** electronic thermal conductivity of Rb_2TlRhF_6

4 Conclusion

The structural, optoelectronic, and thermoelectric characteristics of A_2TlRhF_6 (A=K, Rb) have been ascertained using the most versatile DFT-dependent FP-LAPW technique, which is performed on the basis of the WEIN2K code. Tb-mBJ potential has been employed for evaluating all properties of the examined materials. The structural stability has been confirmed using the minimum energy tolerance factor, and formation energy. The compounds are confirmed to be semiconducting by the band structure and TDOS results, with a direct band gap of 2.98 eV and 2.97 eV at the "L-L" symmetry sites for K_2TlRhF_6 and Rb_2TlRhF_6, respectively. Regarding the optical aspects, Rb_2TlRhF_6 absorb a wide range of absorption of 155–523 nm UV-Visible radiation, which makes it suitable materials for solar cells and optoelectronic applications. The elevated values of ZT, PF, and Seebeck coefficient at room temperature of 300 K, along with the ultralow value of lattice vibration, are very advantageous for thermoelectric generator applications. The value of the figure of merit ZT of 0.99 at a chemical potential of 0.66 eV for K_2TlRhF_6 and 0.99 (2.35 eV) for Rb_2TlRhF_6, at temperature of 300 K has been found. These compounds will give the experimental community a profound understanding of how to apply them in order to boost optoelectronic and solar cell industry.

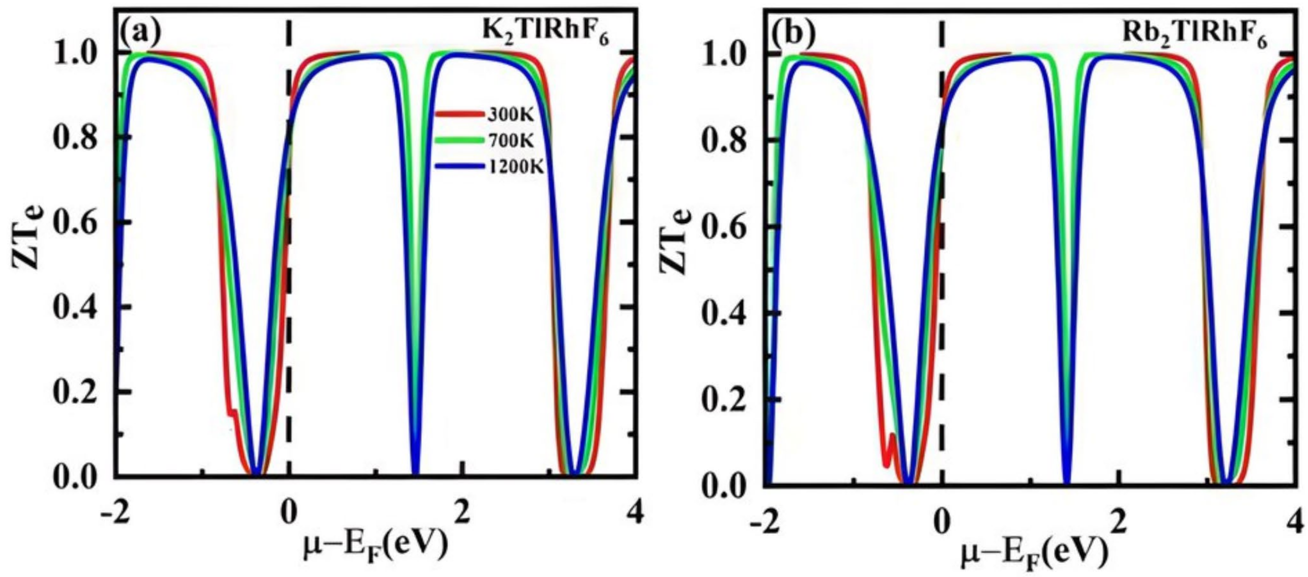

Fig. 12 Computed results of A_2TlRhF_6 (A=K, Rb) with chemical potential using the TB-mBJ approximation **a** figure of merit ZT of K_2TlRhF_6**b** figure of merit ZT of Rb_2TlRhF_6

Acknowledgements The authors present their appreciation to King Saud University for funding this research through the Researchers Supporting Program number (RSPD2024R993), King Saud University, Riyadh, Saudi Arabia.

Author Contributions All persons who meet authorship criteria are listed as authors, and all authors certify that they have participated sufficiently in the work to take public responsibility for the content, including participation in the concept, design, analysis, writing, or revision of the manuscript.Abrar Nazir, Arti Saxena, Mumtaz Manzoor and Ejaz Ahmad Khera- Conceptualization, Methodology, Investigation, Formal Analysis, Software, Writing- Original draft preparation, Supervision.Ahmed Ahmed Ibrahim, Mohammed A. El-Meligy, Barno Abdullaeva and Ramesh Sharma - Writing- Original draft preparation, Visualization, Investigation. Writing- Reviewing and Editing, funding acquisition.

Data Availability No datasets were generated or analysed during the current study.

Declarations

Competing Interests The authors declare no competing interests.

References

1. S. Chu, A. Majumdar, Opportunities and challenges for a sustainable energy future, Nature, **488**, 294–303 (2012)
2. R. Freer, A.V. Powell, Realising the potential of thermoelectric technology: a Roadmap. J. Mater. Chem. C **8**, 441–463 (2020)
3. B. Gajdzik, R. Wolniak, R. Nagaj, B. Žuromskaitė-Nagaj, W.W. Grebski, The influence of the global energy crisis on energy efficiency: a comprehensive analysis. Energies. **17**, 947 (2024)
4. M. Jamil, F. Ahmad, Y. Jeon, Renewable energy technologies adopted by the UAE: prospects and challenges–a comprehensive overview. Renew. Sustain. Energy Rev. **55**, 1181–1194 (2016)
5. C. Tong, Introduction to Materials for Advanced Energy Systems (Springer, 2019)
6. A.G. Olabi, N. Shehata, H.M. Maghrabie, L.A. Heikal, M.A. Abdelkareem, S.M.A. Rahman, S.K. Shah, E.T. Sayed, Progress in solar thermal systems and their role in achieving the sustainable development goals. Energies. **15**, 9501 (2022)
7. R.S. Srivastava, A. Kumar, S. Sharma, H. Thakur, S. Patel, R. Vaish, Development and applications of thermoelectric based dehumidifiers. Energy Build. **252**, 111446 (2021)
8. E.W. Zaia, M.P. Gordon, P. Yuan, J.J. Urban, Progress and perspective: soft thermoelectric materials for wearable and internet-of-things applications. Adv. Electron. Mater. **5**, 1800823 (2019)
9. B. Srinivasan, Novel Chalcogenide Based Glasses, Ceramics and Polycrystalline Materials for Thermoelectric Application (in, Université de Rennes, 2018)
10. K.V. Valavala, Thermoelectric characterization of one-and two-dimensional materials, in, University of Illinois at Urbana-Champaign, (2017)
11. Y. Pei, X. Shi, A. LaLonde, H. Wang, L. Chen, G.J. Snyder, Convergence of electronic bands for high performance bulk thermoelectrics, Nature, **473**, 66–69 (2011)
12. D. Champier, Thermoelectric generators: a review of applications. Energy. Conv. Manag. **140**, 167–181 (2017)
13. S. Chou, W. Yang, K. Chua, J. Li, K. Zhang, Development of micro power generators–a review. Appl. Energy. **88**, 1–16 (2011)
14. F. Vélez, J.J. Segovia, M.C. Martín, G. Antolín, F. Chejne, A. Quijano, A technical, economical and market review of organic Rankine cycles for the conversion of low-grade heat for power generation. Renew. Sustain. Energy Rev. **16**, 4175–4189 (2012)
15. P. Sundarraj, D. Maity, S.S. Roy, R.A. Taylor, Recent advances in thermoelectric materials and solar thermoelectric generators–a critical review. RSC Adv. **4**, 46860–46874 (2014)
16. A. Elghool, F. Basrawi, T.K. Ibrahim, K. Habib, H. Ibrahim, D.M.N.D. Idris, A review on heat sink for thermo-electric power generation: classifications and parameters affecting performance. Energy. Conv. Manag. **134**, 260–277 (2017)
17. R.L. Armstrong, H.M.V. Driel, The observation of incipient phase transitions in K2PtCl6, K2PdCl6, and K2IrCl6. Can. J. Phys. **50**, 2048–2053 (1972)

18. E. Orgaz, M. Gupta, The electronic properties of intermetallic hydrides with the K2PtCl6 structure. J. Phys.: Condens. Matter. **5**, 6697 (1993)
19. M. Huma, M. Rashid, Q. Mahmood, E. Algrafy, N.A. Kattan, A. Laref, A. Bhatti, Physical properties of lead-free double perovskites A2SnI6 (A=cs, rb) using ab-initio calculations for solar cell applications. Mater. Sci. Semiconduct. Process. **121**, 105313 (2021)
20. Q. Mahmood, T. Ghrib, A. Rached, A. Laref, M. Kamran, Probing of mechanical, optical and thermoelectric characteristics of double perovskites Cs2GeCl/Br6 by DFT method. Mater. Sci. Semiconduct. Process. **112**, 105009 (2020)
21. R. Ullah, M.A. Ali, G. Murtaza, A. Khan, A. Mahmood, Ab initio study for the structural, electronic, magnetic, optical, and thermoelectric properties of K2OsX6 (X=cl, br) compounds. Int. J. Energy Res. **44**, 9035–9049 (2020)
22. R. Ullah, M.A. Ali, G. Murtaza, A. Mahmood, S.M. Ramay, The significance of anti-fluorite Cs2NbI6 via its structural, electronic, magnetic, optical and thermoelectric properties. Int. J. Energy Res. **44**, 10179–10191 (2020)
23. S.M. Qaid, H. Murtaza, Q. Ain, M.U. Din, H.M. Ghaithan, A.A.A. Ahmed, J. Munir, The physical attributes of rubidium-based Rb2TlRhF6 double perovskite halide: a first-principles investigation. Phys. B: Condens. Matter. **685**, 416000 (2024)
24. A. Nazir, A. Dixit, E.A. Khera, M. Manzoor, R. Sharma, A. Moayad, A DFT exploration of the optoelectronic and thermoelectric features of a novel halide double perovskite a 2 YAuI 6 (A=rb, Cs) for solar cell and renewable energy applications. Mater. Adv. **5**, 4262–4275 (2024)
25. D. Abdullah, D.C. Gupta, Probing the opto-electronic, phonon spectrum, and thermoelectric properties of lead-free fluoride perovskites A2GeSnF6 (A=K, rb, Cs) for energy harvesting devices. Sci. Rep. **14**, 12644 (2024)
26. S.M. Qaid, H. Murtaza, Q. ul Ain, H.M. Ghaithan, A.A.A. Ahmed, M. Alkadi, J. Munir, A computational approach to correlate the physical attributes of lead-free Rb2XRhF6 (X=Li, Ag) double perovskite halides for optoelectronics and renewable energy applications. Phys. B: Condens. Matter. **671**, 415416 (2023)
27. S.M. Qaid, M. Jamil, J. Munir, H.M. Ghaithan, A.A.A. Ahmed, Q. ul Ain, A computational insight into Rb2ASbX6 (A=tl, Cu & X=I, cl) double perovskites for energy storage and optoelectronic applications. Phys. Scr. **98**, 105910 (2023)
28. J. Munir, M.K. Iftikhar, M.I. Jamil, M.U. Din, T. Alshahrani, H. Elsaeedy, Q. Ain, Physical properties of elastically and thermodynamically stable magnetic AcXO3 (X=cr, fe) perovskite oxides: a DFT investigation. Phys. Scr. **98**, 065513 (2023)
29. H. Murtaza, Q. Ain, J. Munir, H.M. Ghaithan, M. Ali, A.A.A. Ahmed, S.M. Qaid, Tuning the thermoelectric and optoelectronic attributes of lead-free novel fluoroperovskites Cs2BB'F6 (B=rb, in, na and B'= ir, as, rh): a first-principles investigation. J. Phys. Chem. Solids. **190**, 111934 (2024)
30. H. Murtaza, Q. Ain, J. Munir, H. Ullah, H.M. Ghaithan, A.A.A. Ahmed, S.M. Qaid, Unveiling the mechanical, structural, thermoelectric, and optoelectronic potential of K2NaGaBr6 and K2RbTlBr6 double perovskites for sustainable technologies. Sol. Energy. **273**, 112502 (2024)
31. J. Munir, I. Mursaleen, H.M. Ghaithan, Q. ul Ain, A.A.A. Ahmed, S.M. Qaid, First-principles investigations of the mechanically and thermodynamically stable potassium-based double perovskites K2TlAsX6 (X=cl, br) for optoelectronic and renewable applications. Mater. Sci. Eng. B **298**, 116830 (2023)
32. M.Y. Sofi, D.C. Gupta, Scrutinized the inherent spin half-metallicity and thermoelectric response of f-electron-based RbMO3 (M=np, Pu) perovskites: a computational assessment. Sci. Rep. **12**, 19476 (2022)
33. M.Y. Sofi, M.S. Khan, J. Ali, M.A. Khan, Exploring the lead-free halide Cs2MGaBr6 (M=Li, na) double perovskites for sustainable energy applications. Sci. Rep. **14**, 5520 (2024)
34. M.Y. Sofi, M.S. Khan, J. Ali, M.A. Khan, Unlocking the role of 3d electrons on ferromagnetism and spin-dependent transport properties in K2GeNiX6 (X=br, I) for spintronics and thermoelectric applications. J. Phys. Chem. Solids. **192**, 112022 (2024)
35. M.Y. Sofi, A. Ramzan, M.S. Khan, A. Kumar, M.R. Rather, S.A. Sofi, S.A. Khandy, M.A. Khan, Pioneering computational insights into the structural, magnetic, and thermoelectric properties of A3XN (A=Co, Fe; X=cu, Zn) anti-perovskites for advanced material applications. Mater. Sci. Semiconduct. Process. **185**, 108925 (2025)
36. M.Y. Sofi, M.S. Khan, M.A. Khan, Control of spin on ferromagnetism and thermoelectric properties of K 2 GeMnX 6 (X=cl, br, I) halide perovskites: emerging candidates for semiconductor spintronics and thermoelectric applications. Mater. Adv. **5**, 4913–4931 (2024)
37. M.Y. Sofi, M.S. Khan, M.A. Khan, Eco-friendly lead-free halide double perovskites a 2 CuMCl 6 (A=K, rb; M=sb, Bi): stability, thermoelectric, and optoelectronic advancements through theoretical insights. J. Mater. Chem. C **12**, 16045–16058 (2024)
38. M.Y. Sofi, M.S. Khan, J. Ali, M. Ajmal, Khan, Novel thermoelectric material Ba2AlNbO6 for energy harvesting applications, in: International Conference on Nanotechnology: opportunities and Challenges, Springer, 2022, pp. 85–91
39. M.Y. Sofi, M.S. Khan, J. Ali, M.A. Khan, Thermoelectric Response of Vacancy Order Double Perovskite K2PtBr6 for Energy Harvesting Applications (in: Advanced Functional Materials for Sustainable Environments, Springer, 2024), pp. 179–188
40. K.K. Mishra, R. Sharma, A comparative study of the structural, electronic, and optical properties of Ca3SbCl3 halide perovskite using DFT-GGA and HSE06 functional for photovoltaic applications. Opt. Quant. Electron. **57**, 1–19 (2025)
41. K.K. Mishra, Exploring the Physical, Electrical and Optical properties of Cs2LiInBr6 Perovskite: an extensive study utilizing DFT based GGA-PBE and HSE06 functionals. Braz. J. Phys. **55**, 1–14 (2025)
42. K.K. Mishra, Evaluating the potential of Ca3SbBr3 Halide Perovskite for Photovoltaics: a structural, mechanical, and Optoelectronic Study using GGA-PBE and HSE06 functionals. Phys. Solid State. **66**, 464–475 (2024)
43. K. Mishra, Investigation of the double perovskite halides Cs2CuSbH6 (H=cl, br, I): electronic and optical properties for flexible electronics device applications. Phys. Solid State. **66**, 445–458 (2024)
44. K. Mishra, S. Chahar, R. Sharma, An extensive investigation of structural, electronic, and optical properties of inorganic perovskite Ca3AsCl3 for photovoltaic and optoelectronic applications: a first-principles approach using Quantum ATK tool. Solid State Commun. **390**, 115623 (2024)
45. S. Chahar, K.K. Mishra, R. Sharma, Investigation of structural, electronic, and optical characteristics of a novel perovskite halide, Mg3AsCl3, for electronic applications, physica status solidi (b), **261**2400171 (2024)
46. K. Mishra, S. Chahar, R. Sharma, Machine learned analysis of pnictides based Sr3PnCl3 (pn=P, as, sb) halide perovskites for next-generation solar applications. Phys. Lett. A **523**, 129817 (2024)
47. S. Chahar, C. Malan, K.K. Mishra, R. Sharma, Optimizing novel perovskite Mg3AsBr3 through uniaxial stress: a comprehensive study of its potential in solar and optoelectronic applications. Phys. Scr. **99**, 095994 (2024)
48. M. Petersen, F. Wagner, L. Hufnagel, M. Scheffler, P. Blaha, K. Schwarz, Improving the efficiency of FP-LAPW calculations. Comput. Phys. Commun. **126**, 294–309 (2000)

49. P. Blaha, K. Schwarz, G.K. Madsen, D. Kvasnicka, J. Luitz, wien2k, an augmented plane wave + local orbitals program for calculating crystal properties, 60 (2001)
50. M. Ernzerhof, G.E. Scuseria, Assessment of the Perdew–Burke–Ernzerhof exchange-correlation functional. J. Chem. Phys. **110**, 5029–5036 (1999)
51. V. Tyuterev, N. Vast, Murnaghan's equation of state for the electronic ground state energy. Comput. Mater. Sci. **38**, 350–353 (2006)
52. H. Zaari, A. El Hachimi, A. Benyoussef, A.E. Kenz, Comparative study between TB-mBJ and GGA + U on magnetic and optical properties of CdFe2O4. J. Magn. Magn. Mater. **393**, 183–187 (2015)
53. G.K. Madsen, D.J. Singh, BoltzTraP. A code for calculating band-structure dependent quantities. Comput. Phys. Commun. **175**, 67–71 (2006)
54. H. Murtaza, Q. Ain, J. Munir, H.M. Ghaithan, A.A.A. Ahmed, A.S. Aldwayyan, S.M. Qaid, Effect of bandgap tunability on the physical attributes of potassium-based K2CuBiX6 (X = I, br, cl) double perovskites for green technologies. Inorg. Chem. Commun. **162**, 112206 (2024)
55. H. Murtaza, Q. Ain, J. Munir, H.M. Ghaithan, A.A.A. Ahmed, S.M. Qaid, First-principles analysis on the optoelectronic, structural, elastic and transport characteristics of novel fluoroperovskites Cs2TlAgF6 for green technology. ECS J. Solid State Sci. Technol. **13**, 033006 (2024)
56. A. Nazir, E.A. Khera, M. Manzoor, A.A. Ghfar, Y.A. Kumar, H. Ullah, R. Sharma, Screening the structural, optoelectronic and thermoelectric features of novel inverse perovskites X3MgNa (X = cl, br and I): a theoretical investigation. Solid State Commun. 115622 (2024)
57. R. Gautier, X. Zhang, L. Hu, L. Yu, Y. Lin, T.O. Sunde, D. Chon, K.R. Poeppelmeier, A. Zunger, Prediction and accelerated laboratory discovery of previously unknown 18-electron ABX compounds. Nat. Chem. **7**, 308–316 (2015)
58. H. Murtaza, Q. Ain, J. Munir, H.M. Ghaithan, R. Sharma, A.A.A. Ahmed, S.M. Qaid, A comprehensive theoretical analysis of the physical attributes of cesium-based Cs2LiTlCl6 double perovskites for eco-friendly technologies. Phys. B: Condens. Matter. **677**, 415729 (2024)
59. M. Jaiswal, R. Menon, Polymer electronic materials: a review of charge transport. Polym. Int. **55**, 1371–1384 (2006)
60. O. Dolgov, D. Kirzhnits, E. Maksimov, On an admissible sign of the static dielectric function of matter. Rev. Mod. Phys. **53**, 81 (1981)
61. M.U. Din, J. Munir, T. Alshahrani, H. Elsaeedy, Q. Ain, Scrutinized the spin-orbit coupling effect on the elastically and thermodynamically stable Rb2BCl6 (B = pb, Ti) double perovskites for photocatalytic, optoelectronic and renewable energy applications. Mater. Sci. Semiconduct. Process. **163**, 107569 (2023)
62. H. Murtaza, Q. Ain, J. Munir, H.M. Ghaithan, A.A.A. Ahmed, A.S. Aldwayyan, S.M. Qaid, A DFT approach to explore the structural, optoelectronic, mechanical, and thermoelectric attributes of lead-free RbInX3 (X = I, br, cl) halide perovskites for renewable energy applications. Phys. Scr. **99**, 055947 (2024)
63. A. Nazir, E.A. Khera, M. Manzoor, K. Althubeiti, S. Al Otaibi, M. Soliyeva, N. Elboughdiri, H. Ullah, R. Sharma, DFT insights for thermoelectric characteristics of Sr3AsI3 for energy harvesting applications by TB-mBJ studies. Inorg. Chem. Commun. **169**, 113112 (2024)
64. C. Emeis, L. Oosterhoff, G.D. Vries, Numerical evaluation of Kramers—Kronig relations, Proceedings of the Royal Society of London. Series A. Mathematical and Physical Sciences, **297**, 54–65 (1967)
65. E.V. Tsiper, Z.G. Soos, Electronic polarization in pentacene crystals and thin films. Phys. Rev. B **68**, 085301 (2003)
66. J.M. Flores, M. Trainic, S. Borrmann, Y. Rudich, Effective broadband refractive index retrieval by a white light optical particle counter. Phys. Chem. Chem. Phys. **11**, 7943–7950 (2009)
67. J.A. Soares, Introduction to Optical Characterization of Materials, in: Practical Materials Characterization (Springer, 2014), pp. 43–92
68. H. Wang, X. Liang, J. Wang, S. Jiao, D. Xue, Multifunctional inorganic nanomaterials for energy applications. Nanoscale. **12**, 14–42 (2020)
69. R. Singh, S. Dogra, S. Dixit, N.I. Vatin, R. Bhardwaj, A.K. Sundramoorthy, H. Perera, S.P. Patole, R.K. Mishra, S. Arya, Advancements in thermoelectric materials for efficient waste heat recovery and renewable energy generation. Hybrid. Adv. 100176 (2024)
70. E.A. Khera, A. Nazir, M. Manzoor, M. Ayub, F. Hussain, B.A. Al-Asbahi, R. Sharma, First principles exploration of structural stability, optoelectronic and thermoelectric properties of BaXO3 (X = hf, Ti, V) for solar cell applications. Mater. Today Commun. **39**, 108629 (2024)
71. E.A. Khera, H. Ullah, M. Imran, N.A. Niaz, F. Hussain, R.A. Khalil, U. Resheed, A.M. Rana, M.I. Hussain, Mahata, ab initio study of oxygen vacancy effects on structural, electronic and thermoelectric behavior of AZr1-xMxO3 (A = ba, ca, Sr; M = Al, Cu, x = 0.25) for application of memory devices. J. Mol. Graph. Model. **103**, 107825 (2021)
72. A. Nazir, E.A. Khera, M. Manzoor, B.A. Al-Asbahi, Y.A. Kumar, R. Sharma, A density functional theory study of the structural, mechanical, optoelectronics and thermoelectric properties of InGeX3 (X = F, Cl) perovskites, Polyhedron **257**, 117009 (2024)
73. Y.C. Chiu, Y.C. Liaw, Organizational slack: is more or less better? J. Organizational Change Manage. **22**, 321–342 (2009)
74. G.J. Snyder, A.H. Snyder, Figure of merit ZT of a thermoelectric device defined from materials properties. Energy Environ. Sci. **10**, 2280–2283 (2017)
75. H. Alam, S. Ramakrishna, A review on the enhancement of figure of merit from bulk to nano-thermoelectric materials. Nano Energy. **2**, 190–212 (2013)
76. A. Nazir, E.A. Khera, K. Althubeiti, S. Al Otaibi, M. Soliyeva, R. Sharma, M. Manzoor, Impact of halogens modifications on physical characteristics of lead-free hybrid double perovskites compounds Cs2YCuX6 (X = cl, br, and I) for energy storage applications: first principles investigations. Chem. Phys. **588**, 112449 (2025)
77. A.M. Tighezza, A. Nazir, E.A. Khera, M. Manzoor, M. Ishfaq, R. Sharma, A DFT approach to study the vacancy ordered lead free double inorganic perovskites Na2PtX6 (X = cl, br) for sustainable technologies. J. Inorg. Organomet. Polym Mater. 1–18 (2024)
78. K.A. Alrashidi, A. Dixit, A. Nazir, E.A. Khera, S. Mohammad, M. Manzoor, R. Khan, R. Sharma, A DFT Approach to Insight on the Structural, Optoelectronic and Thermoelectric properties of Cubic Perovskites YXO3 (X = Ga, In) for renewable energy applications. J. Inorg. Organomet. Polym Mater. 1–15 (2024)
79. E.A. Khera, A. Nazir, Z. Ahmed, M. Manzoor, H. Ullah, S. Ansar, Y.A. Kumar, R. Sharma, Computational prediction of Structural, Optoelectronic, Thermodynamic, and thermoelectric response of the cubic Perovskite RbTmCl3 via DFT-mBJ + SOC studies, physica status solidi (b), 2400123 (2024)
80. Q. Xiao, A. Nazir, E.A. Khera, M. Manzoor, R. Sharma, J. Rahman, S. Ansar, F. Ali, Probing the opto-electronic, thermoelectric, thermodynamic and elastic responses of lead-free double perovskite Li2ATlCl6 (A = na and K) for potential photovoltaic and high-energy applications: a DFT study. Mater. Sci. Engineering: B **312**, 117860 (2025)
81. A. Nazir, E.A. Khera, M. Manzoor, B.A. Al-Asbahi, R. Sharma, Tunable opto-electronic and thermoelectric response of alkali based half-heusler semiconductors AMgN (A = rb, Cs) for

sustainable energy: a computational approach. Mater. Sci. Engineering: B **303**, 117338 (2024)